Astronomy & Astrophysics manuscript no. 40886corr
October 15, 2021
©ESO 2021

arXiv:2107.01636v2 [astro-ph.CO] 14 Oct 2021

The BINGO project IV:

Simulations for mission performance assessment and preliminary component separation steps

Vincenzo Liccardo*[1], Eduardo J. de Mericia[1], Carlos A. Wuensche[1], Elcio Abdalla[2], Filipe B. Abdalla[1,2,3,4], Luciano Barosi[5], Francisco A. Brito[5,15], Amilcar Queiroz[5], Thyrso Villela[1,6], Michael W. Peel[13,14], Bin Wang[7,11], Andre A. Costa[7], Elisa G. M. Ferreira[2,8], Karin S. F. Fornazier[2], Camila P. Novaes[1], Larissa Santos[7,11], Marcelo V. dos Santos[5], Mathieu Remazeilles[9], Jiajun Zhang[12], Clive Dickinson[9], Stuart Harper[9], Ricardo G. Landim[10], Alessandro Marins[2], Frederico Vieira[1]

[1] Divisão de Astrofísica, Instituto Nacional de Pesquisas Espaciais - INPE, Av. dos Astronautas 1758, 12227-010 - São José dos Campos, SP, Brazil
[2] Instituto de Física, Universidade de São Paulo, 05315-970, São Paulo, Brazil
[3] University College London, Gower Street, London,WC1E 6BT, UK
[4] Department of Physics and Electronics, Rhodes University, PO Box 94, Grahamstown, 6140, South Africa
[5] Unidade Acadêmica de Física, Universidade Federal de Campina Grande, R. Aprígio Veloso, 58429-900 - Bodocongó, Campina Grande - PB, Brazil
[6] Instituto de Física, Universidade de Brasília, Campus Universitário Darcy Ribeiro, 70910-900, Brasília, DF, Brazil
[7] Center for Gravitation and Cosmology, College of Physical Science and Technology, Yangzhou University, Yangzhou 225009, China
[8] Max-Planck-Institut für Astrophysik, Karl-Schwarzschild Str. 1, 85741 Garching, Germany
[9] Jodrell Bank Centre for Astrophysics, Department of Physics and Astronomy, The University of Manchester, Oxford Road, Manchester, M13 9PL, U.K.
[10] Technische Universität München, Physik-Department T70, James-Franck-Straβe 1, 85748 Garching, Germany
[11] School of Aeronautics and Astronautics, Shanghai Jiao Tong University, 200240, China
[12] Center for Theoretical Physics of the Universe, Institute for Basic Science (IBS), Daejeon 34126, Korea
[13] Instituto de Astrofísica de Canarias, 38200, La Laguna, Tenerife, Canary Islands, Spain
[14] Departamento de Astrofísica, Universidad de La Laguna (ULL), 38206, La Laguna, Tenerife, Spain
[15] Departamento de Física, Universidade Federal da Paraíba, Caixa Postal 5008, 58051-970 João Pessoa, Paraíba, Brazil

Received XX, XX, 2020; accepted XX, XX, 2020

ABSTRACT

Aims. The large-scale distribution of neutral hydrogen (HI) in the Universe is luminous through its 21 cm emission. The goal of the **B**aryon Acoustic Oscillations from **I**ntegrated **N**eutral **G**as **O**bservations – **BINGO** – radio telescope is to detect baryon acoustic oscillations (BAOs) at radio frequencies through 21 cm intensity mapping (IM). The telescope will span the redshift range $0.127 < z < 0.449$ with an instantaneous field-of-view of $14.75° \times 6.0°$.
Methods. In this work we investigate different constructive and operational scenarios of the instrument by generating sky maps as they would be produced by the instrument. In doing this we use a set of end-to-end IM mission simulations. The maps will additionally be used to evaluate the efficiency of a component separation method (`GNILC`).
Results. We have simulated the kind of data that would be produced in a single-dish IM experiment such as BINGO. According to the results obtained, we have optimized the focal plane design of the telescope. In addition, the application of the `GNILC` method on simulated data shows that it is feasible to extract the cosmological signal across a wide range of multipoles and redshifts. The results are comparable with the standard principal component analysis method.

Key words. 21-cm cosmology – baryon acoustic oscillations – radio astronomy – BINGO Telescope

1. Introduction

Constraints on the nature and properties of dark energy can be obtained from an accurate description of the Universe's expansion history. Such a description can be provided by standard rulers: objects or properties of known size for which we can easily retrieve the distance-redshift relation (Weinberg et al. 2013). Baryon acoustic oscillations (BAOs), frozen relics of the epoch when matter and radiation were coupled together, are promising standard ruler candidates and could help us understand more about the nature of dark energy (see Albrecht et al. 2006). The current scenario is that, for much of cosmic history, matter dominated over dark energy and the expansion indeed slowed, enabling galaxies and large-scale structures (LSSs) to form. A billion years ago, matter became sufficiently dilute due to expansion, dark energy became the dominant component of the Universe, and the expansion accelerated.

* E-mail: vic2000@hotmail.it

To date, BAOs have only been detected by performing large galaxy redshift surveys in the optical waveband (Eisenstein et al. 2005). However, given the implications of these measurements, it is important that they be confirmed in other wavebands and measured over a wide range of redshifts. The radio band provides a unique and complementary observational window for the understanding of dark energy via the redshifted 21 cm neutral hydrogen emission line from distant galaxies. The **B**aryon Acoustic Oscillations from **I**ntegrated **N**eutral **G**as **O**bservations (BINGO) telescope is a proposed new instrument designed specifically to observe such a signal and to provide a new insight into the Universe (Battye et al. 2013; Abdalla et al. 2021a).

The telescope design consists of two dishes in a compact configuration with no moving parts and will operate in the frequency range from 0.98 GHz to 1.26 GHz (corresponding to a co-moving distance of 380–1280 Mpc/h assuming a ΛCDM cosmology; Planck Collaboration et al. 2020). It will map the cosmic web in three dimensions without detecting individual galaxies, a technique called intensity mapping (IM; Peterson et al. 2006). Instead of cataloging many individual galaxies, one can study the LSS directly by detecting the aggregate emission from many galaxies that occupy large ≈ 100 Mpc^3 voxels. The unresolved 21 cm signal from the galaxies is therefore similar to a low-resolution galaxy survey and can be used as a low-z cosmological probe via BAO measurements. The full-width at half-maximum of the BINGO beam is 40 arcmin, allowing structures of angular sizes corresponding to a linear scale of around 150 Mpc to be resolved (BAOs manifest themselves as a small but detectable excess of galaxies with separations of ≈ 150 Mpc in the chosen redshift range).

Large-scale HI fluctuations above redshift $z = 0.1$ have been unambiguously detected only in cross-correlation with existing surveys of optically selected galaxies (Lah et al. 2009; Chang et al. 2010; Masui et al. 2013). Cross-correlation between the cosmological 21 cm signal and optical surveys provides potentially useful information on the statistical properties of the HI distribution (Switzer et al. 2015). The cross-correlation has the advantage, in comparison to "autocorrelation" studies, that the measured statistics are less sensitive to contaminants such as foregrounds, systematics, and noise. The detection of the redshifted 21 cm radiation will provide valuable information about the post-recombination history of the Universe, including the Dark Ages. Information can also be extracted about the formation of the first ionizing sources and the subsequent reionization of the intergalactic medium (IGM) due to these sources (for a comprehensive review, see Furlanetto et al. 2006 and Pritchard & Loeb 2012).

Broadband foreground emission poses the greatest challenge to 21 cm IM and needs to be characterized carefully before the technique becomes a sensitive probe of the post-recombination epoch ($z < 160$). The foregrounds are expected to be predominantly Galactic and approximately four orders of magnitude larger than the cosmological signal (at low frequencies, synchrotron emissions from our Galaxy and other radio galaxies are the dominant foregrounds; Bigot-Sazy et al. 2015). Therefore, one of the key observational challenges in detecting the cosmological 21 cm signal is modeling and removing Galactic foregrounds at low frequencies. In doing this, the BINGO pipeline adopts the component separation strategies that use the spatial structure of foregrounds to separate them from the cosmological signal. Indeed, the cosmological 21 cm signal is expected to have structure in frequency space, while the foregrounds are expected to mostly be spectrally smooth. Many of these techniques were first developed for cosmic microwave background (CMB) data analysis and are now being extended to IM, where there is the extra dimension of frequency (Ansari et al. 2012; Switzer et al. 2013). There are still spectrally un-smooth emission sources, such as radio frequency interference (RFI) from terrestrial and non-terrestrial sources, that can dominate over Galactic and extragalactic foregrounds. Radio frequency interference can be minimized through software removal, by choosing radio-quiet locations, and through band selection.

This work aims to test and optimize the constructive and operational parameters of the telescope, as well as the data analysis process itself. A set of computational routines and procedures (pipeline) that simulate the BINGO operation has been implemented. Its input is composed of maps of different emission mechanisms, produced by theoretical models or observations, and inherent noise properties of the equipment and the environment. The number and arrangement of horns, optical design, and receiver characteristics are also input parameters of the radio telescope. The IM pipeline produces, as output, time-ordered data sets (TODs) and antenna temperature maps that simulate the signal picked up by the instrument during a given period of operation. Next, these output data are passed through a component separation process for the recovery of the HI component.

The paper proceeds as follows: In Sect. 2 we give an overview of the instrument. In Sect. 3 the pipeline is briefly introduced along with a complementary discussion of the input models, the latest configuration updates, and the component separation method (`GNILC`). Then, in Sect. 4 we study the observational efficiency of different feed horn arrangements. This is followed by the simulations and the component separation results and analysis (Sect. 5). Finally, we present the conclusion, with several future prospects.

Throughout this paper we use cosmological parameters from Planck Collaboration et al. (2020). This is the fourth (IV) of a series of papers describing the BINGO project. The theoretical and instrumental projects are in papers I and II (Abdalla et al. 2021a; Wuensche et al. 2021), the optical design in paper III (Abdalla et al. 2021b), the component separation and correlations in paper V (Fornazier et al. 2021), the simulations for a mock 21 cm catalog are described in paper VI (Zhang et al. 2021), and the cosmological forecasts for BINGO in paper VII (Costa et al. 2021).

2. The instrument

The telescope will be built on a hill near Aguiar, Paraíba (northeastern Brazil). Earlier concepts of the BINGO can be found in Battye et al. (2013) and Wuensche & BINGO Collaboration. (2019). The primary dish will be a 40 m diameter paraboloid and the secondary, a 34 m-diameter hyperboloid. The particular mirror configuration chosen is the crossed Dragone, also known as Compact Range Antenna. Such a design has very low geometric aberrations, leading to an instantaneous field-of-view of ≈ 88 deg^2. It will provide excellent polarization performance and very low side-lobe levels required for HI IM. A detailed description of the project and the instrument is available in companion papers I and II (Abdalla et al. 2021a; Wuensche et al. 2021).

In this paper we compare the two feed horns arrays considered in the current optical design (see Abdalla et al. 2021b): the first one (hexagonal) is composed of 31 units (Fig. 1), while the second one (double-rectangular) is made up of 28 units (Fig. 2). One of the purposes of this work is to investigate, through simulations, which arrangement best meets the scientific goals defined for BINGO.

Each horn will be secured in the focal plane by a hexagonal casing, which works both as a transportation box and assembly

Table 1. Summary of the BINGO Phase 1 telescope parameters.

Description	Value
Dish diameters (m)	40 (primary) 34 (secondary)
Resolution (°)	≈ 0.67
Focal length (m)	63.2
Frequency range (MHz)	980–1260
Channel resolution (MHz)	9.33
Z interval	0.127–0.449
Number of feeds n_f	28
Central focal plane array elevation (°)	≈ 82
Azimuth (°)	0 (North)
Telescope effective area (m^2)	≈ 1120
Pixel solid angle (sr) - Ω_{pix}	0.35
Field of view (deg^2)	14.75×6.0
Survey area Ω_{sur} (deg^2)	≈ 5324
System temperature T_{sys} (K)	≈ 70

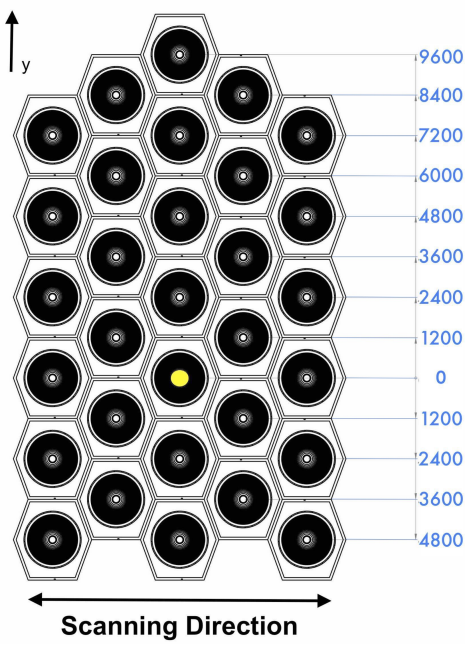


Fig. 1. Hexagonal feed horns array (≈ 9 m × 17 m). The numbers represent the positions of the horns along the y axis, from the center of the field-of-view, given in mm.

cell. It will encapsulate the horn, transitions, polarizer, magic tee, and the receiver box (Wuensche et al. 2021). With this hexagon concept, it is likely that no additional external structure will be needed to position the horn array structure. The hexagonal casing will be 2400 mm tall and will allow moving the horn in elevation y and azimuth x directions, as well as longitudinally z (along the horn optical axis). By means of a pivot attached to the hexagonal case, where the horn is mounted, it will be possible to do a fine positioning of the horns. The aim is to reproduce the desired curvature of the focal plane by translating and tilting the horns across the array. This configuration will improve the sky coverage and final science products. In the future, the structure has the capacity to increase the number of horns to 56 for the double-rectangular array (by adding two extra columns on both sides) and 49 for the hexagonal one (by adding two columns on both sides with five and four horns, respectively, in such a way as to form a hexagon). This will double the redundancy (for the double-rectangular configuration) in the area covered and will increase the sensitivity by $\sqrt{2}$ per year.

3. Simulations and data processing

In this section we briefly describe the data processing and the imaging algorithm used to obtain the BINGO maps. We follow the procedure described by Bigot-Sazy et al. (2015) for an earlier version of BINGO.

To assess the reliability with which the cosmological signal can be extracted from the observed data, an end-to-end simulation pipeline has been developed by the BINGO collaboration, allowing the testing of various aspects of the data analysis pipeline including foreground removal. The input is composed of maps of different emission mechanisms, produced by theoretical models or by observations, as well as by the inherent noise of the instrument and contamination from the environment. Other inputs are features of the telescope, such as the number and arrangement of horns, optical design and receiver characteristics. The pipeline produces as output a time series, which can be turned into maps that simulate the signal picked up by the instrument during a given period of operation.

To detect BAOs in the HI signal, we will need to remove the contributions from much brighter emission coming from our Galaxy and many extragalactic sources (foregrounds). The most relevant emissions at ≈ 1 GHz are a combination of extragalactic point sources and diffuse Galactic synchrotron emission, which taken together is nearly four orders of magnitude larger (≈ 5 K rms at 1 GHz) than the 21 cm signal fluctuations (≈ 200 μK rms) outside of the Galactic plane. Therefore, the output data are passed through a component separation process to recover the cosmological HI component.

In Fig. 3 a flowchart of the BINGO simulation pipeline is shown. In blue are the "configurable" parameters of the simulation: instrument specifications (beam shape and number of horns, observation time, knee frequency, number of channels, etc.) and component separation (method and parameters). In red are the parameters that have already been measured (the instrument noise module and the CMB temperature are already included in the pipeline). In yellow are the modules that make use of known models and observations to produce emission maps used as input in the simulations. The RFI part of the pipeline currently only deals with simulating the emissions from the Global Navigation Satellite System (GNSS), and a new module is currently under development to include fixed location terrestrial RFI. The atmosphere appears as a source of large-scale black-body emission with a brightness temperature of a few K at around 1 GHz. The atmospheric brightness temperature has been calculated according to the model in Paine (2019), and we found, assuming an air temperature of 284 K, that the value is approximately 4 K at the zenith.

The pipeline operation makes use of a mission simulator, which processes all the input information described above to produce TODs. In the case of BINGO, this data set consists of the temperature measurements in a given channel i in the range 980–1260 MHz, in a given celestial coordinate (α, δ) and at a given time of observation t_{obs}. As BINGO is a telescope without

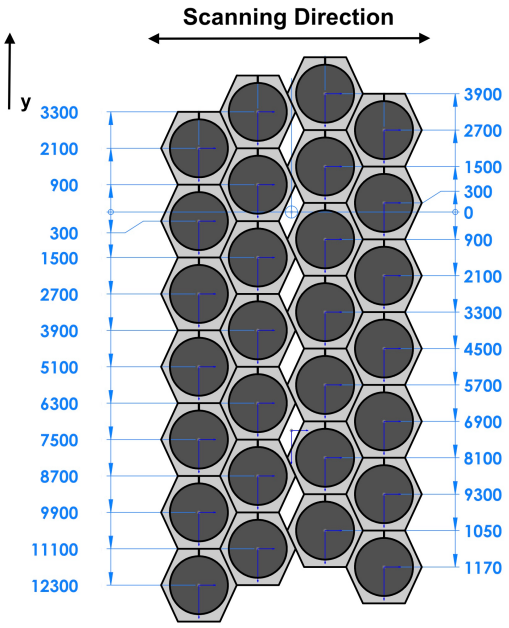


Fig. 2. Double-rectangular feed horns array (≈ 7.8 m × 18.6 m). The numbers represent the positions of the horns along the y axis, from the center of the field-of-view, given in mm.

moving parts, each pixel will visit n times the same coordinate (α,δ), where n depends on the instrument operating time. Then, for every frequency channel in each horn, the TOD is processed into a map using the `HEALPix` pixelization scheme (Górski et al. 2005).

By default, each pixel in the `HEALPix` map is filled with the mean value of all measurements in that pixel according to equation

$$T_{\rm map}(\alpha,\delta) = \sum_{t=0}^{t} \langle T_t\,(\alpha_t,\delta_t)\rangle\,, \tag{1}$$

where t is the measurement time and T_t is the temperature measured at that time in the coordinates (α,δ). After this step, which is done separately for each horn, the horn maps are combined into the final cube of BINGO maps. Eventually, as a separate task from the operation of the pipeline, the set of maps produced by the simulation is processed through a component separation algorithm to recover the cosmological HI signal from the data produced by the pipeline.

This work aims to simulate the results to be obtained by the Phase 1 BINGO instrument configuration and to test a new component separation method developed for the Planck mission (`GNILC`), following the results obtained in Olivari et al. (2016). A number of different configurations of the instrument are investigated.

3.1. The cosmological signal

The idealized observed brightness temperature of the sky, $T_{\rm sky}(\nu,\phi)$, at frequency ν and direction ϕ, is given by

$$\begin{aligned} T_{\rm sky}(\nu,\phi) = T_{\rm gal}(\nu,\phi) + T_{\rm eg}(\nu,\phi) + T_{\rm CMB}(\nu,\phi) \\ + T_{\rm atm}(\nu,\phi) + T_{\rm COSMO}(\nu,\phi)\,, \end{aligned} \tag{2}$$

where $T_{\rm gal}$ is the diffuse Galactic radiation, $T_{\rm eg}$ is the emission from extragalactic sources, $T_{\rm CMB}(\nu,\phi)$ is the CMB temperature, $T_{\rm atm}(\nu,\phi)$ is the atmosphere emission, and $T_{\rm COSMO}$ is the cosmological HI emission. In what follows we briefly describe the cosmological HI emission model used for the simulations.

The HI brightness temperature has been simulated with the *Full-sky Lognormal Astro-fields Simulation Kit* (`FLASK`; Xavier et al. 2016). `FLASK` can generate fast full-sky simulations of cosmological LSS observables such as multiple matter density tracers (galaxies, quasars, dark matter halos), CMB temperature anisotropies and weak lensing convergence and shear fields. The multiple fields can be generated tomographically in an arbitrary number of redshift slices and all their statistical properties (including cross-correlations) are determined by the angular power spectra supplied as input and the multivariate lognormal (or Gaussian) distribution assumed for the fields. After generating the fields, `FLASK` can apply selection functions and noise to them.

The HI emission at low redshifts ($z \lesssim 0.5$, much later than the end of reionization era) is assumed to be confined to discrete elements such as galaxies, bubbles, and filaments. In this case, the HI signal is characterized by a mean HI brightness temperature given by (Hall et al. 2013)

$$T_b = 188\,h\,\Omega_{\rm HI}\frac{(1+z)^2}{E\,(z)}{\rm mK}\,, \tag{3}$$

where $E(z) = (H(z)/H_0)$, $H_0 = 100h$ km s^{-1} Mpc (where h is the Hubble parameter) and $\Omega_{\rm HI}$ is the density parameter for HI. This is the HI assumed value for all papers in this BINGO series. The fluctuations around this mean are due to differences in densities of structure. Once the HI signal is assumed to be a tracer of the dark matter, these fluctuations can easily be calculated.

Using the HI angular power spectra we produce full-sky maps of the HI signal with the help of the `synfast` routine of `HEALPix`. However, with the `FLASK` software, we can assume a log-normal distribution for the HI signal. In doing this, we used the C_ℓs from the *Unified Cosmological Library for C_ℓs* code (`UCLCL`; McLeod et al. 2017; Loureiro et al. 2019) as input for `FLASK`. `UCLCL` is a library for computing two-point angular correlation function of various cosmological fields that are related to LSS surveys. It uses the formalism of angular power two-point correlations and then derives the exact analytical equations for the angular power spectrum of cosmological observables. The auto- and cross-correlations between different observables as well as different galaxy populations (bins) can also be computed.

The simulated full-sky HI signal for this work includes 30 redshift bins of 21 cm intensity fields for BINGO, equally spaced in frequency, following the fiducial BINGO parameters. The HI density fields are generated from discrete matter tracers (galaxies) from the DES photometric survey (Flaugher 2005). The photo-z distribution for DES galaxies has been estimated from Sánchez et al. (2014). The mean temperature of the HI signal fluctuations in the BINGO redshift range is $\approx 200\,\mu$K. We set `HEALPix` resolution of the map equal to $N_{\rm side} = 128$, which corresponds to a map pixel size of 27 arcmin.

In Fig. 4 the resulting HI map from the `FLASK` code at 1.1 GHz (the central frequency of BINGO bandwidth) is shown. Due to the discrete tracers field that emits the HI signal, the measured auto-spectra have a shot noise contribution as well as a clustering contribution. To correctly predict the overall HI signal, this contribution must be accounted for in our HI simulation. The shot noise depends on the abundance of galaxies observable in our hypothetical survey, and assuming a comoving number density sources $n = \frac{dN}{dV} = 0.03h^3Mpc^{-3}$, the angular density of the

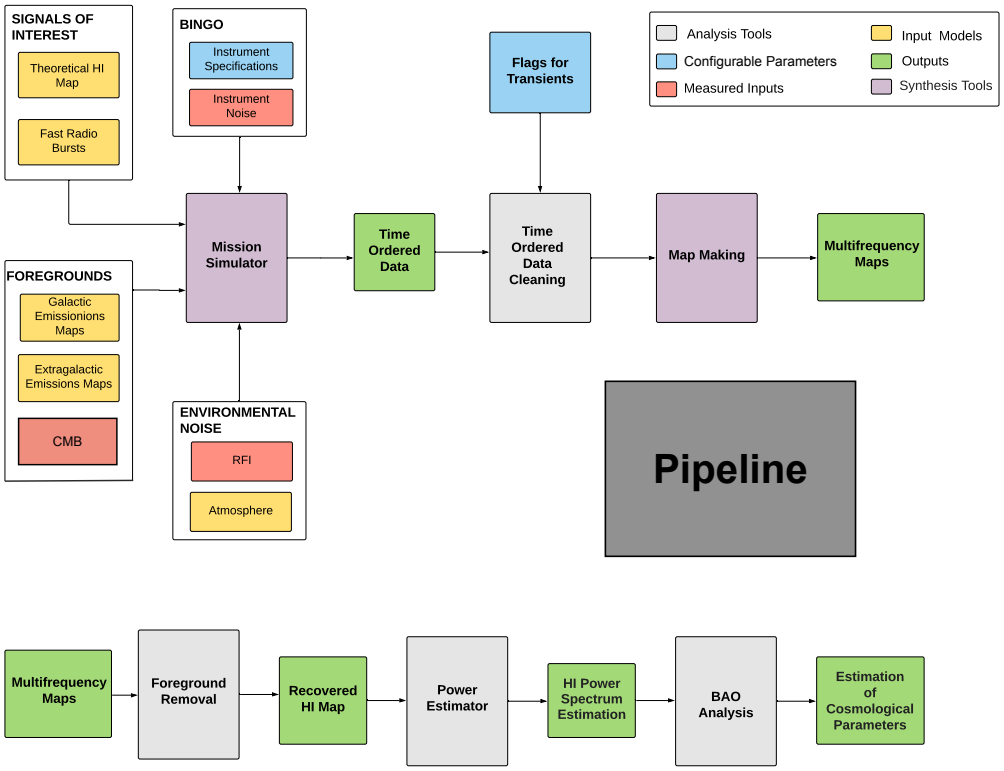


Fig. 3. BINGO mission simulation flowchart.

sources can be expressed as

$$\bar{N}(z) = 0.03h^3 \frac{c}{H_0} \int \chi^2(z) \frac{dz}{E(s)} . \quad (4)$$

Then, the shot noise contribution to the 21 cm power spectrum is subtracted, assuming assuming a Poisson behavior,

$$C_\ell^{\rm shot} = \frac{1}{\bar{N}(z)} . \quad (5)$$

3.2. Foregrounds

An accurate understanding of the foreground emission is essential in order to precisely determine the cosmological HI signal. Usually, the principal source of uncertainty is the contamination by foreground emission from the Galaxy, rather than the instrumental noise itself. Three different types of Galactic foregrounds have been included in the present version of the pipeline: synchrotron, free-free emission and anomalous microwave emission (AME; Fig. 4). Extragalactic radio sources, which are an inhomogeneous mix of radio galaxies, quasars and other objects, are being implemented as a separate module in the code.

However, besides the diffuse Galactic emission and the extragalactic radio sources, the CMB also contributes as a contaminant to the HI signal. In the BINGO frequency band, the antenna noise temperature and the CMB temperature are of the same order of magnitude ($h\nu/k_BT \ll 1$). Therefore, at BINGO frequencies, the CMB radiation represents nearly a constant background (fluctuations of $\approx 100\ \mu$K) of 2.7 K. The fluctuations themselves, can be removed by having a spatial CMB template from WMAP/Planck (Planck Collaboration et al. 2020), which can then be removed directly from the data (after convolution with the BINGO beam).

For the sake of comparison, in the companion paper V (Fornazier et al. 2021) the foreground maps are generated directly from the *Planck Sky Model* (PSM) package. They include as input synchrotron, free-free and AME (same as the options in this work) as well as the contribution of a background of radio sources, which we considered less important in a first stage due to the angular scale of our pixelization.

In the following subsections, we briefly describe the specific Galactic foregrounds used in this work and how we simulate them. Further details about the Galactic and extragalactic foregrounds are given in companion paper I (Abdalla et al. 2021a).

3.2.1. Galactic synchrotron

It is well known that synchrotron radiation arises from interactions between cosmic ray electrons and magnetic fields in the Galaxy. Since the magnetic fields in our Galaxy extend far to the outskirts of the Galactic plane, synchrotron emission can also be measured at high Galactic latitudes, making it difficult to avoid by only excluding the Galactic plane regions from the analysis. The frequency scaling of synchrotron flux emission is often approximated in the form of a power law, $I_\nu \propto \nu^\epsilon$, over a limited range of ν. In terms of Rayleigh-Jeans brightness temperature, we have $T \propto \nu^\gamma$, with $\gamma = -(\epsilon + 3)/2$. A typical value is $\gamma \approx -2.5$ at radio frequency (De Oliveira-Costa et al. 2008), and takes steeper values $\gamma \approx -3.0$ at $\approx$10 GHz frequencies. Full-sky continuum maps in the low-frequency range are available, for example, the Haslam map (Haslam et al. 1982) at 408 MHz and the 1.4 GHz map by Reich & Reich (1986).

For our simulations, we used the reprocessed Haslam 408 MHz all-sky map from Remazeilles et al. (2015). This includes

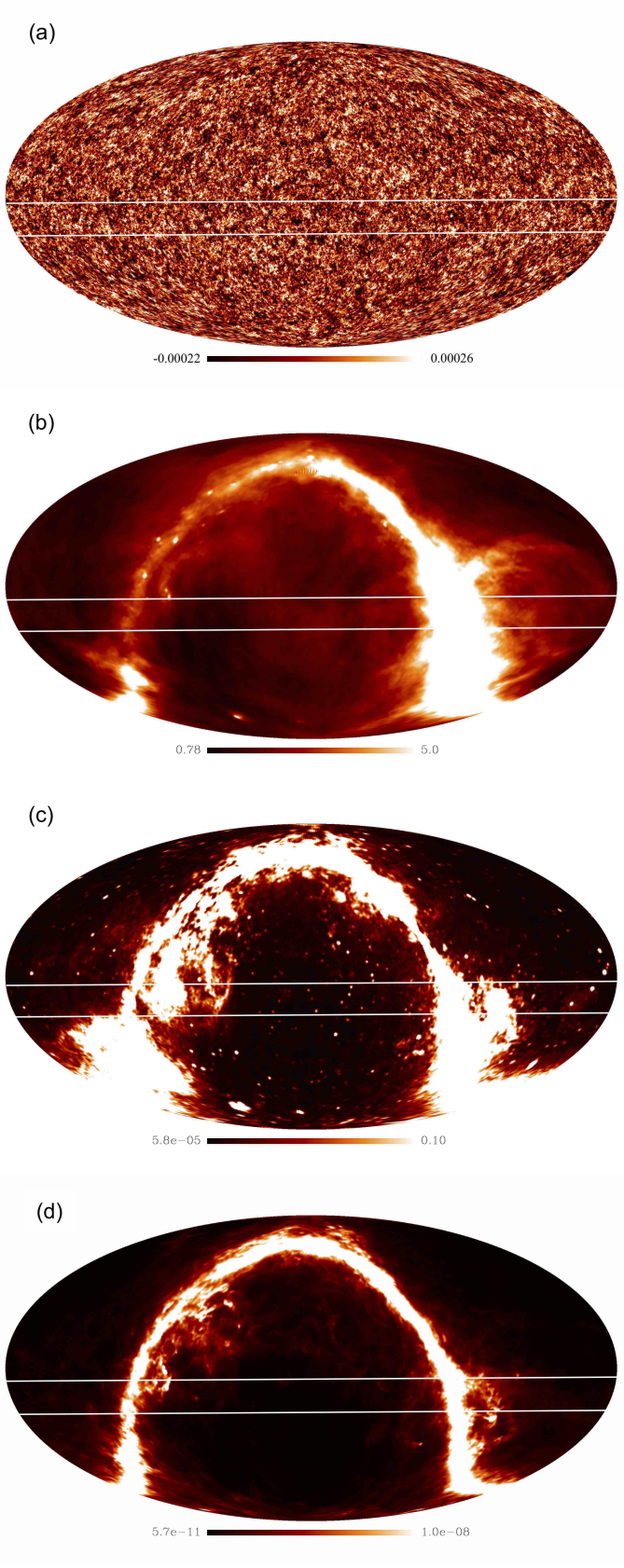


Fig. 4. Full-sky maps of the cosmological signal and the different foregrounds for a frequency slice $\nu \approx 1.1$ GHz: (a) extragalactic HI, (b) synchrotron, (c) free-free, and (d) AME. The stripe defined by the white solid lines is the sky region covered by BINGO. We selected different temperature intervals for the maps to show their features and to allows the comparison of temperature differences at first inspection. Temperatures are given in K.

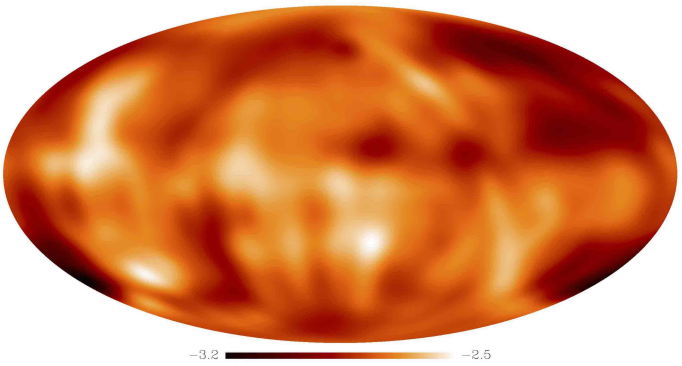


Fig. 5. Map of the synchrotron spectral index according to the Giardino model.

artificially added small-scale fluctuations as described by Delabrouille et al. (2013). We consider that the synchrotron spectral index is spatially variable according to the Giardino model (Giardino et al. 2002), which was derived using the full-sky map of synchrotron emission at 408 MHz from Haslam et al. (1982), the northern hemisphere map at 1420 MHz from Reich & Reich (1986) and the southern hemisphere map at 2326 MHz from Jonas et al. (1998). In the Giardino model, the synchrotron spectral index has a mean value of -2.9 and a standard deviation of 0.1 (Fig. 5) and is good for frequencies $\lesssim 2.3$ GHz. Our choice here differs from companion paper V (Fornazier et al. 2021), who use the PSM synchrotron sky with the synchrotron spectral index distribution produced by Miville-Deschênes et al. (2008).

The observed diffuse synchrotron emission at radio frequencies is distributed across the entire sky as shown in the point-source subtracted all-sky map in Fig. 4. Most of the synchrotron emission from the Galaxy is concentrated along the Galactic plane, but large-scale features such as Loop I stretch over around half of the north Galactic sky.

3.2.2. Free-free

Since, in the BINGO frequency interval, free-free radio continuum emission is subdominant to other Galactic emission types such as synchrotron emission it is very challenging to uniquely isolate a map of radio free-free emission. Therefore, generating free-free emission maps of the whole sky mostly relies upon the use of tracer emissions. However, free-free maps can also be produced by component separation techniques (e.g., Adam et al. 2016), which could be used here in the future.

At optical wavelengths, the emission from the Hα transition can be used as a tracer of free-free (Dickinson et al. 2003). Optical Hα continuum maps can be easily related to free-free emission at radio wavelengths in regions with a small Hα optical depth ($\tau < 1$), which is limited to the sky far from the Galactic plane. We use the Hα map by Dickinson et al. (2003) as a template for the Galactic free-free emission. This map includes small-scale fluctuations as described in Delabrouille et al. (2013). The free-free spectrum can be well defined by a power law with a temperature spectral index $\beta = -2.1$ (Dickinson et al. 2003),

$$T_{\rm ff} \approx 10\,{\rm mK}\left(\frac{T_e}{10^4\,{\rm K}}\right)^{0.667}\left(\frac{\nu}{\rm GHz}\right)^{-2.1}\left(\frac{I_{H\alpha}}{\rm R}\right), \quad (6)$$

which flattens the spectral index of the total continuum of our Galaxy where the free-free has a brightness temperature comparable to that of the synchrotron emission. T_e is the electron

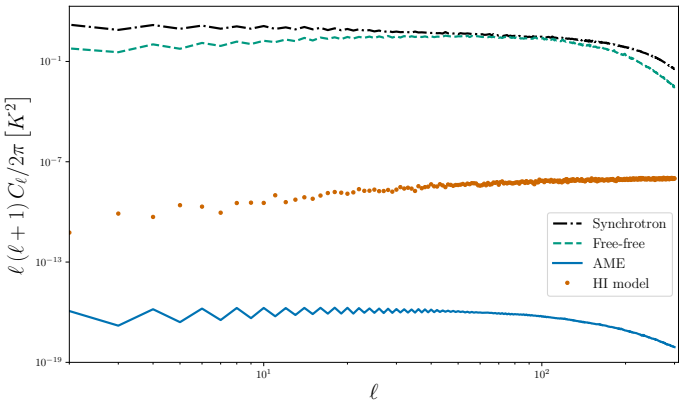


Fig. 6. Angular power spectra of the cosmological signal and the different foreground components at $\nu \approx 1.1$ GHz.

temperature in K, and $I_{H\alpha}$ is the H_α template whose emission is given in Rayleigh (R).

In the BINGO observation region, the free-free brightness temperature fluctuations are ≈ 0.25 mK; therefore, they are considerably weaker than the synchrotron component but significantly brighter than the HI fluctuations (Battye et al. 2013). The final free-free template at 1.1 GHz is shown in Fig. 4.

3.2.3. Anomalous microwave emission

Anomalous microwave emission is diffuse Galactic radiation detected at frequencies between 10 GHz and 60 GHz (Dickinson et al. 2018). The best accepted physical process for the production of AME is the spinning dust model, which proposes that the rapid rotation of the electric dipoles associated with the smallest dust grains in the interstellar medium can generate microwave frequency emission that peaks between 10 and 60 GHz.

To simulate the AME emission, we used as a template the *Planck* τ_{353} optical depth map (Planck Collaboration et al. 2016b). We adopted the factor $8.3 \times 10^6\ \mu K/\tau_{353}$ to convert the dust optical depth at 353 GHz to the AME temperature at 22.8 GHz, in units of μK (Planck Collaboration et al. 2016a). To scale the AME emission from 22.8 GHz to the BINGO frequencies of ≈ 1 GHz, we used the publicly available `spdust2` code (Silsbee et al. 2011), which calculates the spinning dust emissivity as a function of frequency for various environments of the interstellar medium. Anomalous microwave emission temperature fluctuations are extremely weak ($\approx 2\,\mu$K) at frequencies below 10 GHz and are negligible in the frequency range of BINGO (Fig. 6), but we included them for completeness. The final AME template at 1.1 GHz is shown in Fig. 4.

3.3. Instrumental noise

3.3.1. Thermal noise

Phase 1 of BINGO will provide a large field-of-view, and the fine-tuning in the positioning of the 28 horns will improve the overall sensitivity of the experiment. The parameters that affect the sensitivity are the survey area $\Omega_{\rm sur}$, the beam size $\theta_{\rm FWHM}$, the number of horns n_f, and the integration time $t_{\rm obs}$. The r.m.s. noise per pixel is given by the well-known radiometer equation (see Wilson et al. 2013):

$$\sigma_t = \frac{T_{\rm sys}}{\sqrt{t_{\rm pix}\delta\nu}}\,, \tag{7}$$

Table 2. Thermal noise amplitude for different numbers of horns (considering a 100% duty cycle).

Array - Number of feeds	Integration time (yr)	σ_t (μK)
Double-rectangular - **28**	1 (2)	30 (21)
Hexagonal - **31**	1 (2)	29 (20)
Double-rectangular - **56**	1 (2)	15 (11)
Hexagonal - **49**	1 (2)	16 (11)

with $\delta\nu$ as the frequency bin width and t_{pix} the observation time per pixel related to the total observing time by

$$t_{\rm pix} = t_{\rm obs} n_f \frac{\Omega_{\rm pix}}{\Omega_{\rm sur}}\,, \tag{8}$$

where $\Omega_{\rm pix}$ is the pixel solid angle. Equation 8 shows that increasing the field-of-view results in higher r.m.s noise, whereas adding more horns reduces it. The compromise option is determined by the balance between the cosmic variance and systematic effects that dominates the error at large scales and the thermal error dominated at small scales. The cosmic variance error can be reduced with a larger sky coverage. The thermal noise amplitude of the instrument σ_t has been calculated according to the number of horns (Eq. 8). Table 2 presents the estimated sensitivities for the scenarios considered in this study, as well as values for other cases.

In theory, in order to improve the constraints on the acoustic scale k_A, we require a larger field-of-view. However, a larger focal plane area likely brings with it more systematic errors. The criteria is the uncertainty on the acoustic scale k_A, related to the constraints on the measurements of the BAO features. Following the analysis carried out in Battye et al. (2013), if we consider one central redshift $z = 0.3$ it is possible to probe the acoustic scale k_A with a fractional error of 2.4% with 2000 deg^2 and 50 horns. We find that increasing the number of horns from 50 to 70 and the survey area from 2000 deg^2 to 4000 deg^2 gives a measurement of the acoustic scale k_A with accuracy 2.0% (Fig. 7). In order to determine the optimal concept, there is a balance to find between the cosmic variance and $1/f$ noise that dominates the error at large scales and the thermal error dominated at small scales (Blake & Glazebrook 2003; Seo et al. 2010). The latter can be reduced with larger field-of-view and number of horns. At large scales the limitation on the accuracy on the measured power spectrum due to the sample variance can be improved by larger survey volume, and so more sky coverage. However, we have to take into account the systematics induced by a larger focal plane area. Optical simulations show that going further away from the center of the focal plane induces a slightly loss in terms of performance of the beam (ellipticity, gain). In this case, the configuration with ≈ 50 horns and 5000 deg^2 field-of-view represents a good compromise ($\delta\, k_A/k_A \approx 2.1\%$). During Phase 1, BINGO will operate with 28 horns and we intend to add 28 more in Phase 2.

3.3.2. $1/f$ noise

The term $1/f$ noise refers to the type of noise with a power spectrum density (PSD) of the form $S(f) \propto 1/f^\alpha$ where the spectral index α identifies specific types such as pink noise ($\alpha = 1$) and red noise ($\alpha = 2$). In most cases, α is equal to 1. The frequency taken into account for the noise is the inverse of the observation

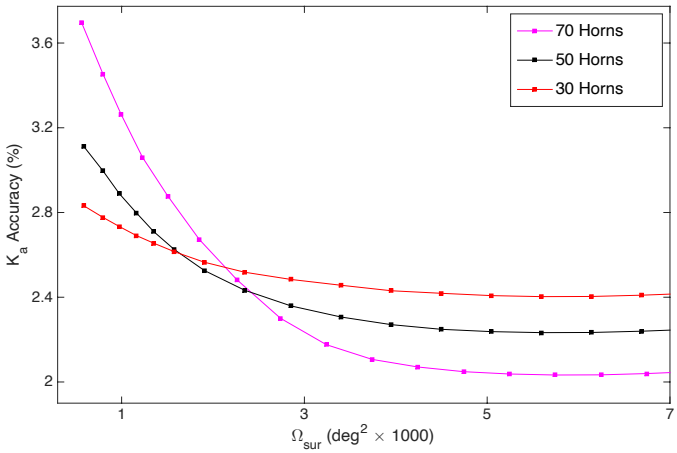


Fig. 7. Uncertainty on the acoustic scale for 30, 50, and 70 feeds based on a one-year observation time and $\theta_{\rm FWHM} = 40$ arcmin.

time ($f = 1/t_{\rm obs}$). Even though it is widely observed in a broad range of scientific areas, a fundamental description of $1/f$ noise is yet to be found. In the case of BINGO, the $1/f$ noise is produced by gain fluctuations of the amplifiers and therefore it is expected to be strongly correlated across all frequency channels.

It is common in astronomy to define the PSD of a receiver contaminated with thermal and $1/f$ noise as follows: for a system with knee frequency f_k (defined as the frequency to which thermal and $1/f$ noise have the same PSD value), system temperature $T_{\rm sys}$, the PSD of the noise fluctuations is given by a power-law model (Harper et al. 2018)

$$S\left(f,\omega\right) = \frac{T_{\rm sys}^2}{\delta\nu}\left[1 + C\left(\beta, n_{ch}\right)\left(\frac{f_k}{f}\right)^{\alpha}\left(\frac{1}{\omega\Delta\nu}\right)^{\frac{1-\beta}{\beta}}\right], \tag{9}$$

where ω is the Fourier mode of the spectroscopic frequency ν, $\Delta\nu$ is the total bandwidth of the receiver and $C(\beta,N_\nu)$ a normalization factor given by $(N_\nu - 1)/(2N_\nu\delta\nu)$, $\delta\nu$ is the channel bandwidth and α is the spectral index of the correlated noise. The spectral index β describes a $1/f$ noise identical in every receiver channel ($\beta \approx 0$) and a noise that is independent in every channel ($\beta = 1$). For an ideal receiver, f_k should be 0 meaning that the receiver TOD is dominated by flat power-spectrum thermal (white) noise only. The thermal and $1/f$ noise are both simulated from independent noise realizations. The stability of the BINGO noise properties can be quantified by the variation in the white noise, knee frequency and spectral index over the lifetime of the experiment. The presence of $1/f$ noise in an observation map introduces stripes following the scan circle strategy (Maino et al. 2002), and its main effect is to increase the uncertainty of measurements on large spatial scales. This striped structure appears because the mean level of the noise is, in general, different for each circle of measurements, as shown by Janssen et al. (1996). It is important to note the difference to the companion paper V approach, where the details of the instrument observation strategy are not considered. Their analysis does include the $1/f$ component but not the β factor, which accounts for correlations across the frequency channels.

In these simulations, the $1/f$ noise fluctuations are assumed to be small multiplicative variations around the system temperature and Gaussian distributed. The 1/f noise can be represented in the TOD as

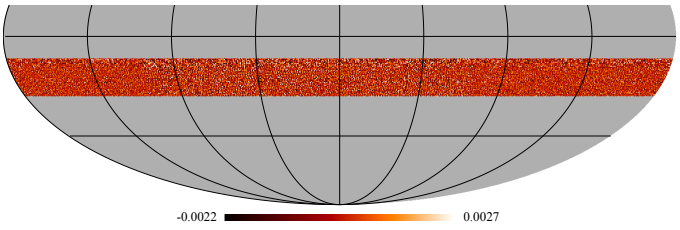


Fig. 8. Simulated $1/f$ noise map of the BINGO observational region. The striped structure is reduced after the filtering of the data. The scale quantifies fluctuations δT around the average in K.

$$\Delta T\left(t,\nu\right) = \delta G\left(t,\nu\right) T_{\rm sys}\left(t,\nu\right), \tag{10}$$

where $\Delta T\left(t,\nu\right)$ is the power of the $1/f$ fluctuations at time t and frequency ν, which is the combination of the instantaneous fluctuation in the gain δG and system temperature $T_{\rm sys}$. The PSD of δG can be described by two parts. The first part is the power spectrum of the temporal fluctuations as in Eq. 9 but without the thermal noise component

$$P(f) = \frac{1}{\delta\nu}\left(\frac{f_k}{f}\right)^{\alpha}, \tag{11}$$

while the second component of the $1/f$ power spectrum describes the correlations of the noise in frequency, and may be described by a conservative power-law model

$$F\left(\omega\right) = \left(\frac{\omega_0}{\omega}\right)^{\frac{1-\beta}{\beta}}, \tag{12}$$

where ω is the Fourier mode of the spectral frequency (i.e., the wavenumber), ω_0 is the smallest wavenumber ($1/\Delta\nu$), and β describes the frequency correlation. The simulated gain fluctuations should be interpreted as ripples across the 2D observed region.

In Fig. 8 we show a $1/f$ map (there is no thermal noise) of the BINGO region using the 28 horn double-rectangular array. When $\beta = 1$, the frequency spectrum is entirely uncorrelated. This means that the number of modes needed to describe the $\beta = 1$ $1/f$ noise is equal to the number of channels; therefore, removing the $1/f$ noise will be very challenging for typical component separation methods (see Sect. 5.2). For the simulation in Fig. 8 we assumed a spectral index $\beta = 0.25$ and the same value of $f_k = 1$ mHz for each receiver and for a 9.33 MHz channel bandwidth. The index α is assumed to be 1, while β and f_k were obtained from preliminary measurements, at Jodrell Bank Observatory, of the statistical properties of the noise using data from the BINGO test correlation receiver (Evans 2017). The $1/f$ noise has been filtered on timescales of ≈ 6 minutes, which is the time structures with the angular scales of interest take to drift across the field-of-view of one horn. This assumes that $1/f$ noise is fully calibrated out (e.g., using a calibration diode) on such timescales, and represents an optimistic scenario.

A good front end for a radio telescope designed for IM with the required stability will exhibit a low knee frequency, ideally on the order of one thousandth of a hertz. The use of correlation

receivers using colfets as reference sources in the BINGO telescope will allow for efficient accounting of the $1/f$ noise contribution (see Wuensche et al. 2021). To reduce the stripe contamination in the maps, we need to carefully measure the relative gains of the individual receivers and determine the beam contribution for each horn before combining the signals from all the beams.

4. Observational strategy

In the radio band the natural tracer of LSSs is the 21 cm line of HI, but the volume emissivity associated with this line is low, meaning that detecting individual galaxies at z ≈ 1 requires a very substantial collecting area. Interferometer arrays are likely to be the best approach to probing higher redshifts at z ≈ 1, where an angular resolution of ≈ 0.1° is required. Using a single dish, moderate-sized telescope with an ultra-stable receiver system, is the lowest-cost approach to IM measurements of BAOs at low redshifts (Battye et al. 2013) and intermediate angular scales. The idea is to exploit the broad beam at low-frequencies to carry out IM (Peterson et al. 2006; Masui et al. 2013) and consequently measure the overall integrated HI brightness temperature of a large number of galaxies, taken together as a tracer of the LSS. Detecting signals of ≈ 200 μK with a non-cryogenic receiver of standard performance implies that every pixel in our intensity map requires an accumulated integration time of > one day over the course of the observing campaign. The total integration time can be built up by many returns to the same patch of sky, but between these, the receiver gains need to be stable. The Galactic emission is known to be significantly polarized. The synchrotron emission, for instance, is polarized up to 40-50% (Wolleben, M. et al. 2006). The linearly polarized part of the Galactic emission will undergo Faraday rotation as it travels through the Galactic magnetic field and the interstellar medium. This means that the observations need to be made with clean beam(s) with low side-lobe levels and very good polarization purity in order to add foreground degrees of freedom.

For the following analysis, we chose a declination strip that minimizes the contribution from Galactic foregrounds. We assume that the telescope will map a ≈ 15° declination strip centered at δ = -17.5° as the sky drifts past the telescope. The need to resolve structures of angular sizes corresponding to a linear scale of around 150 Mpc in our chosen redshift range implies that the required angular resolution has to be about 40 arcmin. As the Earth rotates, each BINGO horn observes a ring at a single declination set up by the instrument geometry. One complete ring is scanned in 24 hours, which is the periodicity of the sky signal. Therefore, a set of periodic rings (one per horn) with 24 hours each, is a standard representation of the BINGO data. The arrangement of feed horns in the focal plane has been optimized in such a way as to cover the ≈ 15° declination strip and at the same time to have some redundancy, that is to say, beams have some superposition with beams of adjacent horns (as shown in Fig. 2). This will increase the signal to noise ratio.

The positioning of each horn is defined by two parameters. The first is the Cartesian (x,y) coordinates of the horn in the focal plane and the second is the elevation and azimuthal angles (el, az). Horns located in the outermost regions of the array are slightly tilted with respect to the focal plane to under-illuminate the secondary mirror and to reduce sidelobes and ground contaminations. The details of the BINGO optical design are given in Abdalla et al. (2021b). In this work, we assume two different horn configurations from that paper: the hexagonal (Fig. 1) and the double-rectangular (Fig. 2) formats. The beams are well approximated by a Gaussian shape and are diffraction-limited.

Different observation times have been tested to understand how they affect the HI signal recovery. The uniformity of the sky coverage will depend on the pixel size used. Since our observation method relies upon the sky drifting across the focal plane, we guarantee a complete (and uniform) sky coverage for BINGO allowing for N independent lines-of-sight, with the resolution of each pixel in the final map being ≈ 15°/N. Both arrangements are good enough when mapping the sky using `HEALPix` with $N_{\rm side}$ = 64 (larger pixels). This $N_{\rm side}$ roughly corresponds to pixels of size 54 arcmin, which avoids missing pixels. This means the effective beam of BINGO will be broader, but by about 30% However, gaps will appear in the sky coverage (declination direction) when the resolution is increased to the real BINGO resolution $\theta_{\rm FWHM}$ = 40 arcmin.

Other arrangements have been analyzed like the ones from Battye et al. (2013) and Bigot-Sazy et al. (2015) or with 60 horns placed equidistantly along the vertical axis, and in such a way as to cover ≈ 15° in total. However, the sky coverage obtained with the above-mentioned options and a resolution $N_{\rm side}$ = 128 (27' pixels) leaves gaps between data stripes, with unobserved regions at constant declination. There are three possible ways of overcoming the problem. Only use `HEALPix` with maximum $N_{\rm side}$ = 64 to produce the maps, change the declination coverage by varying the pointing of the full focal plane, or build a focal plane with more horns. The last option is not possible for financial reasons. Changing the declination coverage can be accomplished by moving all horns vertically at different steps. Five different horn vertical positions are allowed inside the 2400 mm tall hexagonal case. These vertical displacements should happen in such a way as to minimize declination separation between adjacent horns, meaning vertical positions change in the focal plane as a whole (all horns should be placed in the same "new" position), as opposed to elevation and azimuth displacements, which may occur for individual units. Maximum displacement is ± 300 mm for the focal plane.

We simulated the resulting BINGO coverage after displacing all the horns up and down in the focal plane every year by ± 150 mm steps. In doing this, we generated hits maps (meaning how many times a given pixel is scanned) relative to the central channel, which corresponds to the frequency interval 1110.67–1120.00 MHz. All maps are created with $N_{\rm side}$ = 128 and then degraded to BINGO resolution ($\theta_{\rm FWHM}$ = 40 arcmin). The "five elevation" summed maps are equivalent to five years of observations. The resulting maps are shown in Fig. 9 and Fig. 10. The horn repositioning strategy results in a more homogeneous covered area (we found 25% more coverage than the fixed elevation option for the hexagonal format and 12% more coverage for the double-rectangular), which will allow us to obtain a more uniform signal-to-noise ratio per pixel and a better recovery of the overall HI signal. Regarding the two arrangements, we found differences in terms of sky coverage and uniformity. The declination strip is ≈ 15° for the hexagonal array, whereas in the case of the double-rectangular is ≈ 17.5° (≈ 17% larger).

The better sky coverage uniformity achieved with the double-rectangular array is clearly visible in Fig. 11, where the minimum number of observations per pixel (hits) as a function of the covered area (`HEALPix` pixel) is shown. The peaks of the hexagonal arrangement are due to feed redundancy along the scan direction (i.e., pixels seeing the same sky each day) since there are more horns aligned in cross-elevation. It is clearly visible how different feed arrays can affect the uniformity in the sky coverage. The strategy of displacing the horns vertically, re-

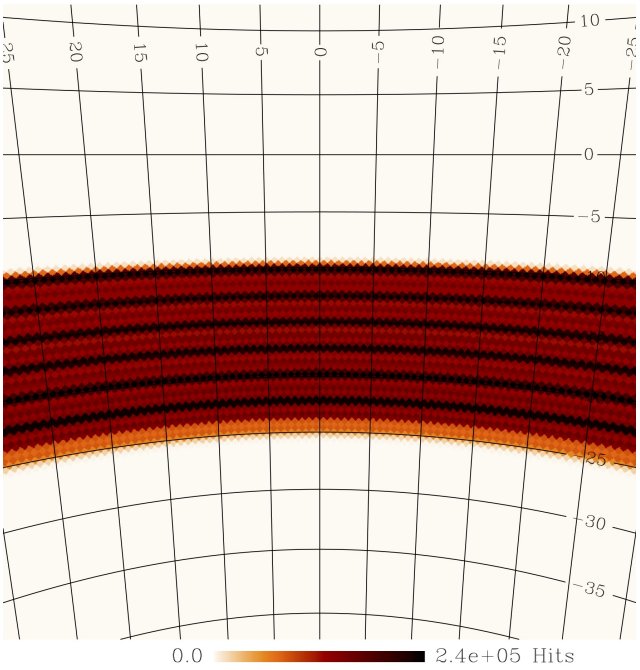


Fig. 9. Gnomonic projection centered at δ = -17.5°, RA = 0 of the BINGO sky coverage when using the hexagonal arrangement with 31 feed horns, after 5 years of mission.

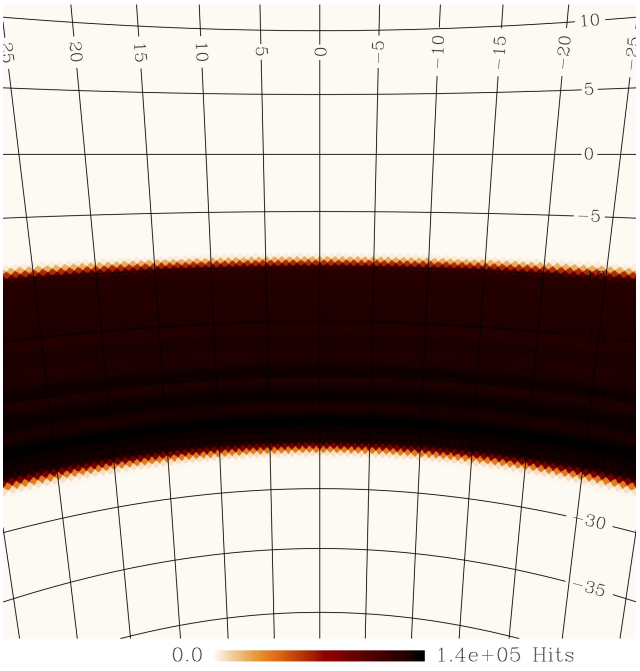


Fig. 10. Gnomonic projection centered at δ = -17.5°, RA = 0 of the BINGO sky coverage when using the double-rectangular arrangement with 28 feed horns, after 5 years of mission.

configuring the focal plane, allow us to avoid gaps in the sky coverage. Better results might be obtained with larger vertical displacements, but the actual geometry of the supporting structure prevents this option.

In terms of noise power spectrum, there is additionally an impact when the observation time of the N horns is not uniformly spread over a fraction of the sky. It is worth noting that the noise power spectrum of an homogeneous coverage is independent of the pixel size used to produce the map. In the case of inhomogeneous coverage, the noise power in a spherical harmonic transform (computed from the harmonic coefficients of the noise map, excluding pixels that are not observed) is

$$N_\ell = 4\pi \times \left\langle \sigma_t^2 \right\rangle / N_{\rm pix} = \frac{4\pi}{N_{\rm pix}} \times \sum_p \left[\frac{\sigma^2_{\rm noise}}{\tau_{\rm obs}\,(p)} \right], \tag{13}$$

where $N_{\rm pix}$ is the total number of pixels in the map, $\tau_{\rm obs}(p)$ is the total time spent observing pixel p (summing-up the time of observation by all horns) and $\sigma_{\rm noise}$ is the white noise level

$$\sigma_{\rm noise} = \frac{T_{\rm sys}}{\sqrt{\delta\nu}}\,. \tag{14}$$

Hence, the amplitude of the noise power spectrum increases when the time distribution is not uniform. When the inhomogeneity is not too large, such an increase remains small. We found a noise level $\approx$ 7% greater when the sky is scanned with the hexagonal horn configuration compared to the double-rectangular arrangement and $N_{\rm side} = 128$. However, as the $N_{\rm side}$ of the maps is increased, big gaps appear and the noise level can reach values of $\approx$ 70% (in the extreme case where half of the pixels are observed five times more often than the other half).

In the double-rectangular configuration, two rows of detectors are shifted compared to the original first two rows of detectors by a one-quarter height of the hexagon height, whereas in the hexagonal configuration the difference in horn heights between the first and the second columns represents half the hexagonal height. This indicates we can reach a better than Nyquist configuration (i.e., having a number of samples per beam equal to two) with the double-rectangular array by simply shifting the position of the horns once during the survey lifetime. Since the shifting occurs each year of the survey, we can obtain a map that is over-sampled in the y direction compared to Nyquist sampling. This will allow us to use other techniques to extract further resolution from the maps such as the drizzle technique applied to `HEALPix` maps (Paradis et al. 2012). Finally, we can say the double-rectangular array give a better noise distribution, which is good for the quality of the data that can be expected from BINGO, but reduces the redundancy.

5. Component separation

5.1. GNILC

The signal measured by a radio telescope is the composition of cosmological signals emitted in the early Universe (e.g., CMB or cosmological HI signal), astrophysical sources emitting in the late Universe (e.g., Galactic foregrounds and extragalactic point sources) and systematic noise of the instrument (e.g., thermal and $1/f$ noise). A component separation process aims to extract the signal of interest from the measured signal by evaluating the correlations of the measurements at different frequencies using physical emission models. This process is extremely important for HI IM experiments, since the detected signal is typically smaller than the Galactic foreground contribution by a factor of roughly 10^{-4}. In addition to these components, systematic contributions can also be removed during the separation process.

Several component separation techniques are available in the literature concerning foreground removal, in particular for CMB data. For instance, the principal component analysis (PCA) technique was successfully employed in the detection of HI at z

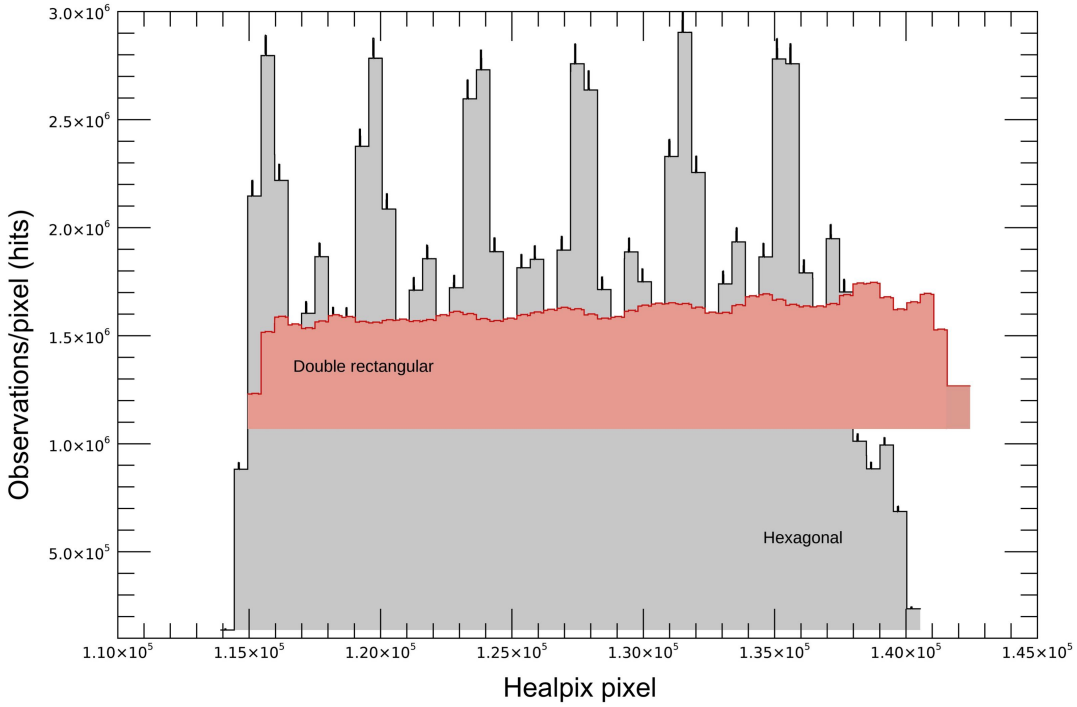


Fig. 11. Sky coverage for BINGO observing strategy (pixel size = 40 arcmin). The histograms represent the sky coverage obtained with the hexagonal (*gray*) and the double-rectangular (*red*) arrangement. The histograms have been obtained with five different horn positionings (± 300 mm, ± 150 mm and 0) considering one year of integration for each elevation. On the y axis we have the number of observations relative to each pixel of the map.

= 0.8 by cross-correlation using the Green Bank 100 m Telescope (Switzer et al. 2013). The Generalized Needlet Internal Linear Combination (GNILC; Remazeilles et al. 2011), is a component separation method developed for the *Planck* collaboration and applied to IM experiments by Olivari et al. (2016). For this method, a data set containing the measurements of intensity (or temperature) $x_i(p)$ at a given frequency i and at a given pixel p can be represented by

$$x_i\,(p) = s_i\,(p) + n_i\,(p)\,, \tag{15}$$

where $s_i(p)$ is the map of the cosmological signal to be recovered and $n_i(p)$ is the map of foregrounds emission and instrumental noise. Equation 15 can be also written as a $1 \times n_{ch}$ vector, where the n_{ch} is the number of channels (frequency bins)

$$\mathbf{x}\,(p) = \mathbf{s}\,(p) + \mathbf{n}\,(p)\ . \tag{16}$$

In this work what is assumed to be the noise are the foregrounds plus the $1/f$ component. HI and thermal noise are about the same order of magnitude in some multipole scales and so, as we try to recover HI, some thermal noise will be recovered as well. In the GNILC method a set of windows ("needlets") is defined in harmonic space so that specific different ranges of angular scales of the input map are isolated. Needlets are a particular construction of wavelets family that can be interpreted as band-pass filters, $h_l^{(j)}$, in harmonic space and can be defined such that

$$\sum_j \left[h_l^{(j)}\right] = 1\,, \tag{17}$$

where j defines an interval of multipoles. The a_{lm} harmonic coefficients are filtered and transformed back into a map, so the statistical information contained there is only relative to a certain range of angular scales. It means that, for each frequency map, there are several needlet maps. This step permits a more localized analysis of the signal. Next, the data covariance matrix $\mathbf{R}$, whose dimensions are $n_{ch} \times n_{ch}$, is defined at pixel p by

$$\mathbf{R}\,(p) = \mathbf{R}_{\rm HI}\,(p) + \mathbf{R}_n\,(p)\ , \tag{18}$$

where $\mathbf{R}_{\rm HI}\,(p) = \langle \mathbf{s}\,(p)\ \mathbf{s}^T\,(p)\rangle$ is the HI covariance matrix, and $\mathbf{R}_n\,(p) = \langle \mathbf{n}\,(p)\ \mathbf{n}^T\,(p)\rangle$ is the covariance matrix of the noise (foregrounds plus $1/f$). The number of components representing the observation data is limited to the number of channels of the experiment, n_{ch}. The foreground components are frequency correlated, so that the foreground signal plus noise $\mathbf{n}$ can be represented by a linear combination of m independent vectors.

The signal to be recovered can be estimated by

$$\hat{\mathbf{s}} = \mathbf{W}\mathbf{x}\,, \tag{19}$$

where $\mathbf{W}$ is the $n_{ch} \times n_{ch}$ weight matrix and $\mathbf{x}$ the data vector described in Eq. 16. The matrix $\mathbf{W}$ minimizes the total variance of the estimated vector $\hat{\mathbf{s}}$, under the condition $\mathbf{WS} = \mathbf{S}$, so that

$$\mathbf{W} = \mathbf{S}\left(\mathbf{S}^T\mathbf{R}^{-1}\mathbf{S}\right)^{-1}\mathbf{S}^T\mathbf{R}^{-1}\,, \tag{20}$$

where $\mathbf{S}$ is the estimate HI plus noise mixing matrix. In order to use Eq. 20 to recover the signal of interest, it is necessary to estimate the $\mathbf{S}$ matrix. To achieve this aim, a theoretical power spectrum of HI is used to determine the local ratio between the cosmological signal and the total observed signal. At this point, we

Table 3. Simulation parameters.

Parameter	Value
Beam resolution (°)	0.67
Observation time (yr)	1, 2
Frequency range (MHz)	980 - 1260
Number of feeds n_f	28, 56
Number of channels n_{ch}	30
Knee frequency (Hz)	0.001
$1/f$ spectral index β	0.001, 0.12, 0.25, 0.6
$T_{\rm sys}$ (K)	70

have an estimate for the reconstructed signal $\hat{\mathrm{s}}$ for each needlet scale. Finally, for each frequency channel, the needlet maps are added to give a complete GNILC recovered HI plus thermal noise map.

5.2. Results

Most of the pipeline is written in the Python programming language. Maps are generated using the HEALPix pixelization scheme. The code simulates the $1/f$ noise-contaminated TODs used for generating maps. Time-ordered data sets with correlated $1/f$ noise properties result in images containing stripes along the telescope drift directions that can dominate the astronomical signal. A set of simulations has been used to test the performance of the BINGO telescope and the quality of the component separation method.

The GNILC method is also investigated in the BINGO paper V (Fornazier et al. 2021) with contaminants generated from the PSM code. In this paper, the efficiency of GNILC in reconstructing HI plus thermal noise maps in the presence of contaminants (already described in this work) is analyzed in respect of how the change of $1/f$ parameters, number of feed horns and observation time influence this process. To estimate the dimension of the HI plus noise subspace in its PCA step, GNILC makes use of theoretically known HI plus noise power spectra (or HI plus noise template maps). The reason for using the HI signal plus the instrumental thermal noise as the signal of interest is that these two emissions, for most of the current IM experiments, are roughly of the same order of magnitude for some of the scales of interest (smaller scales or higher multipoles). Therefore, even when we try to recover the HI signal alone, we end up recovering some thermal noise as well at these scales. This, however, is not an optimal reconstruction of the HI plus noise signal, since GNILC will try to remove as much noise as possible from the data. To avoid creating artificial artifacts on the noise maps, the most efficient strategy for HI IM is then to recover both the HI and noise signals as one single component.

We used a galaxy mask, similar to the GAL70 Planck HI mask, with a cosine apodization of 3° to avoid boundary artifacts in the power spectrum estimation. All maps are generated with $N_{\rm side} = 128$. Table 3 shows the instrumental parameters used for the simulations. Some values have been modified in each tested scenario, such as the observation time, the number of feed horns and the $1/f$ spectral index. The number of channels has been limited to $n_{ch} = 30$. This is a compromise between the increase in the thermal noise amplitude (Eq. 7), computational processing time and the improvement in the GNILC performance with an increase in the number of channels.

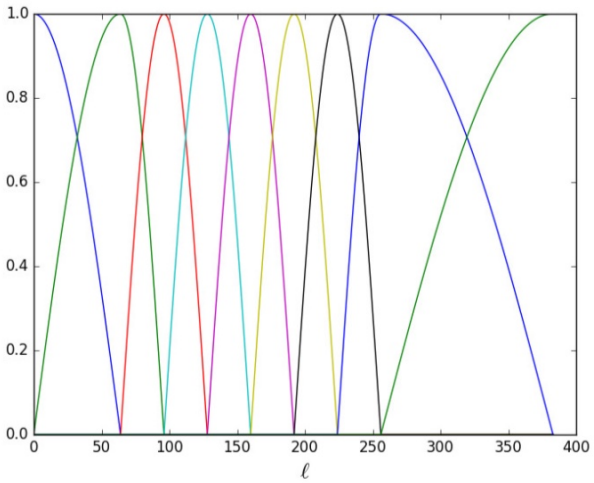


Fig. 12. Particular set of needlets used in this work. A needlet is a tool that permits a certain range of multipoles (or physical scales) to be isolated for the benefit of a particular analysis or procedure.

The GNILC method has two dependences that must be set before the component separation is performed: the set of needlets and the internal linear combination (ILC) bias b. These parameters control the localization that is made by GNILC when calculating the covariance matrices. Needlets determine the location in harmonic and real (or pixel) space. The most appropriate set of needlets for BINGO maps is the one that combines the strengths from a mild localization at low multipoles and a fine localization at high multipoles. Figure 12 shows the set adopted in our analysis. The ILC bias, however, is not a totally free parameter, as its increase leads to an increase in the artificial anticorrelation between the component of interest and the contaminants. It should, therefore, be made as small as possible without increasing the resulting localized area of the sky and computational processing too much.

In order to test the sensitivity of the method as a function of the simulation parameters, we attempted to recover the power spectra for scenarios with a different number of feeds (double-rectangular 28 and 56 and hexagonal 31), different $1/f$ noise correlations and different observation times. To have a quantitative measure of the ability of the GNILC method, we compare the results with the standard PCA method, which is commonly used in HI IM simulations (Bigot-Sazy et al. 2015; Alonso et al. 2014). The PCA method consists of the transformation of the independent maps of each frequency channel into orthogonal modes of the covariance matrix between frequencies. This method relates the foreground components to the eigenvectors with the largest variance modes, which are called the principal components. These principal components are then removed from the data.

As a way to quantify the recovery performance of the methods, the average absolute difference between the input C_ℓ^s and the reconstructed power spectrum C_ℓ^R normalized by the input power spectrum is considered:

$$N_{Rec} = \frac{1}{N_\ell n_{ch}} \sum_i^{n_{ch}} \sum_\ell^{\ell_{\rm max}} \left| \frac{C_\ell^R(\nu_i) - C_\ell^S(\nu_i)}{C_\ell^S(\nu_i)} \right|, \tag{21}$$

where N_ℓ is the total number of multipoles considered and ν_i specifies a frequency channel. The ideal scenario would be when

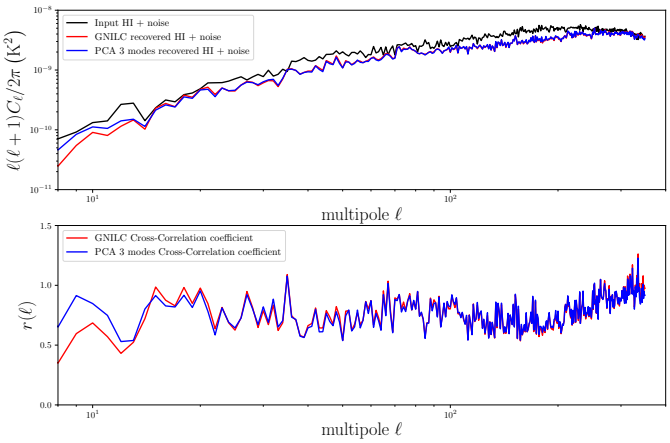


Fig. 13. Component separation results using the simulation pipeline. *Top*: Angular power spectra for the input HI plus noise signal (*black*), the GNILC recovered HI plus noise signal (*red*), and the PCA recovered HI plus noise signal with three modes removed (*blue*) at ≈ 1.1 GHz. For this particular channel and configuration (double-rectangular, 28 feeds, one-year observation time, and $\beta = 0.25$), N_{Rec} (GNILC) equals 21.43%. *Bottom*: Cross-correlation coefficient $r(\ell)$ among the recovered signals (GNILC and PCA) and the input signal.

Table 4. Average normalized absolute difference between the input power spectrum and the recovered power spectrum of the HI plus noise signal (N_{Rec}) for the central frequency (≈ 1.1 GHz) with $\beta = 0.25$. "D.R." stands for "double rectangular" and "HEX" for 'hexagonal arrays."

Number of feeds	28 (D.R.)			31 (HEX)	56 (D.R.)
Integration time (y)	1	2	5	1	1
N_{Rec} **(%)** GNILC	21.43	20.12	14.31	21.05	19.6
N_{Rec} **(%)** PCA	20.37	18.93	12.87	20.13	18.2

$N_{Rec} = 0$, indicating a perfect HI plus noise map reconstruction. We summarize, in Table 4, the values of N_{Rec} obtained for each configuration. All the results shown have been obtained with the same value of the ILC bias (0.01). For the choice of needlets, we used a set that combines, as mentioned before, the strengths from a mild localization at low multipoles and a fine localization at high multipoles. Regarding the standard PCA, the recovery of the HI signal with the smallest bias is obtained when we choose the number of principal components to be equal to 3.

Measurements made with a digital back-end for an earlier version of the BINGO receiver yielded $\beta \approx 0.25$, which we use as our fiducial value. The power spectral density of the spectral gain fluctuations is modeled as a power law and characterized by the parameter β. Small values of β (< 0.25), or high correlation, are preferred, as this makes it easier to remove the 1/f fluctuations using current component separation techniques. The value for β is heavily dependent on the receiver setup. For our analysis, we considered the frequency that is closest to the middle point of the BINGO band.

Figure 13 shows the power spectra of the input HI plus noise signal and the GNILC and PCA recovered HI plus noise signal, relative to the scenario with 28 feeds and one-year observation time. In the bottom panel of Fig. 13 we plot the cross-correlation coefficient, defined as

$$r(\ell) = \frac{C_\ell^R(\nu_i)\, C_\ell^S(\nu_i)}{C_\ell^S(\nu_i)\, C_\ell^S(\nu_i)}. \quad (22)$$

Table 5. N_{Rec} values for different ranges of multipoles (double-rectangular, 28 feeds, one-year observation time, and $\beta = 0.25$) obtained with GNILC at ≈ 1.1 GHz.

Range of multipoles	N_{Rec}
15–30	0.18
30–60	0.28
60–90	0.19
90–120	0.23
120–150	0.30
150–180	0.31
180–210	0.31
210–240	0.22
240–270	0.14
270–300	0.12
300–330	0.08

The cross-correlation coefficient is a complementary way to measure the signal recovery sensitive to scale-dependent signal loss. Depending on the number of principal components that are removed, the PCA either underestimates the HI power spectrum or is contaminated by residual foregrounds. The best result was obtained with 3 modes removed. We can see that the recovery of the two methods is comparable throughout the entire range of multipoles $\approx 12 < \ell < 330$. The performance also depends on the range of angular scales. The cross-correlation coefficient is < 1 throughout almost the entire range of multipoles, while on smaller scales its value increases, showing that the recovered spectrum is contaminated. The GNILC recovered and residuals maps covering the BINGO sky region for this scenario are shown in Fig. 14.

For the three different configurations, the input power spectrum is recovered with good accuracy, with an improvement as the number of feeds is increased (Table 4). The results show that the component separation method does not affect significantly the wanted signal statistics, but it underestimates the power spectrum (Fig. 13). We show in Fig. 15 the values of N_{Rec} (GNILC) obtained for each channel. Performances are worse at the edges of the frequency band, where there is less freedom for the method to fit for the independent components of emission without compromising the reconstruction of the wanted signal.

We finally summarize the GNILC performance for different multipole ranges in Table 5 (scenario with 28 feeds and one-year observation time). The difference between the total signal and the HI plus noise signal is largest in the middle part of the interval, where the Galactic foregrounds are more intense. For smaller scales ($\ell > 200$) instead, we can recover the cosmological HI plus noise power spectrum with very good accuracy. This happens because in this range of scales the difference in power between the total signal and the wanted signal is smaller. It is worth noting that the GNILC performance may be adjusted by changing the ILC bias, whose value represent the localization in the real space. There is a direct dependence on it when the localization in the spherical space is not fine enough. We are investigating this aspect for a future publication.

In this context, we used the GNILC method as well to investigate the impact of $1/f$ noise correlation in the reconstruction of HI plus thermal noise signal. Table 6 shows the results when

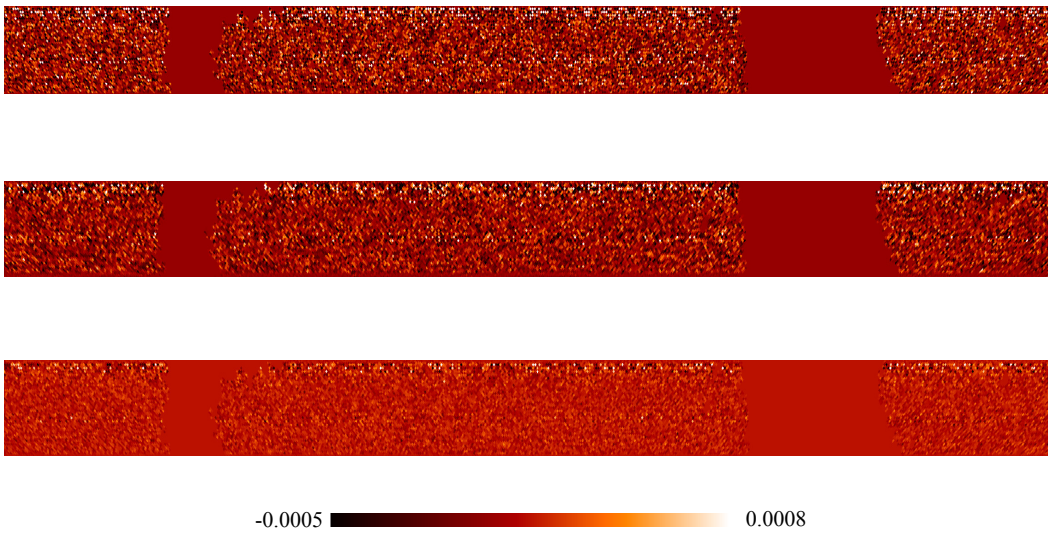


Fig. 14. BINGO HI plus noise maps with a Galactic mask applied at ≈ 1.1 GHz (double-rectangular, 28 feeds, one-year integration time, and $\beta = 0.25$). In the *top* panel we have the input map, in the *middle* panel the GNILC recovered map, and in the *bottom* panel the residuals map (temperatures are given in K).

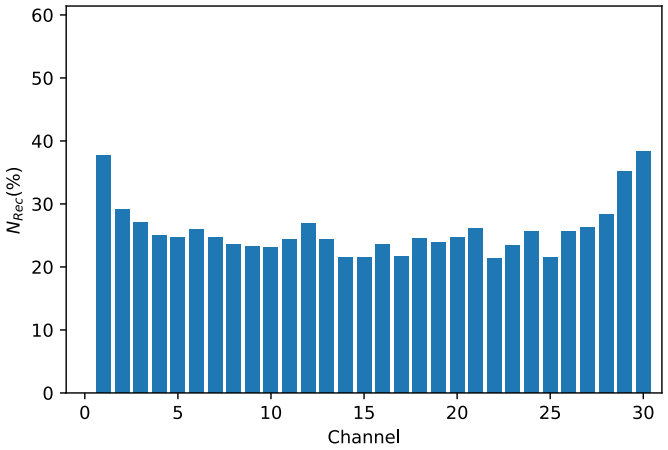


Fig. 15. Histogram showing the average absolute difference between the input and the recovered HI power spectrum normalized by the input HI power spectrum (N_{Rec}) obtained with GNILC for each channel of the BINGO frequency band.

varying β. It can be noted that the degree of $1/f$ noise correlation between the receivers channels affects the recovery of the input power spectrum. According to these results, the GNILC method is capable of recovering the spectrum but with different performances. Our analysis shows that, with real data, the $1/f$ noise contribution will be the more challenging contaminant to be removed. Figure 16 shows the GNILC and PCA recovered HI plus noise power spectra when there is a high degree of $1/f$ noise correlation ($\beta = 0.001$, D.R. 28 feeds, one-year observation time). As expected, an improvement in the GNILC performance with an increase of correlation in frequency is found. The $1/f$ noise can be sufficiently reduced to be significantly lower than the thermal noise based on a one-year observation time with the same instrumental parameters described in Table 3. Further improvements could also be achieved by using more advanced map-making codes. There are some discussed in the literature (e.g., Natoli et al. 2001; de Gasperis et al. 2016) that should be able to suppress in part the $1/f$ noise. For the real observations the 1/f noise effect in the data can be diminished in two ways: either by using very stable receivers so that the knee frequency is reduced or by increasing the scanning speed so that the signal is shifted to higher frequencies. For a static telescope like BINGO this implies that the receiver gains need to be as stable as possible.

Table 6. N_{Rec} for different β values (double-rectangular, 28 feeds, one-year observation time) obtained with GNILC at ≈ 1.1 GHz.

Spectral index	N_{Rec}
0.001	0.12
0.12	0.2
0.25	0.21
0.6	0.32

6. Conclusions

BINGO is a transit telescope designed to make the first detection of BAOs at radio wavelengths, through the detection of the 21 cm HI emission and, consequently, the construction of a 3D map of total matter distribution. In this way, the telescope will provide independent cosmological data to complement optical surveys at the redshift interval $0.127 < z < 0.449$.

We have performed an optimization analysis to determine the best solution for the BINGO focal plane arrangement. Two different arrays have been considered, and other possible configurations can be found in previous works (Battye et al. 2013; Bigot-Sazy et al. 2015). According to the results obtained in this work, the optimal solution for the BINGO focal plane design is the double-rectangular array. This design concept will use a large structure to mount an array of 28 horns, allowing the displacement of each horn along the vertical axis (elevation axis). The structure will be able to host, in the future, up to 56 horns.

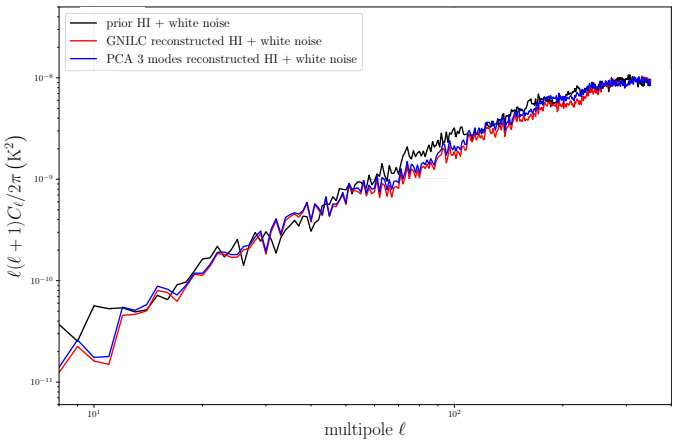


Fig. 16. Angular power spectra for the input HI plus noise signal (*black*), the GNILC recovered HI plus noise signal (*red*), and the PCA recovered HI plus noise signal with three modes removed (*blue*) at ≈ 1.1 GHz. For this particular channel and configuration (double-rectangular, 28 feeds, one-year observation time, and $\beta = 0.001$), N_{Rec} (GNILC) equals ≈ 12 %. The recovery improvement, due to the increased $1/f$ noise correlation, is clear.

In this work we have presented, for the first time, results from the application of the GNILC method to a set of end-to-end simulations generated with the IM pipeline developed by the BINGO collaboration. The foreground cleaning method did show satisfactory results with the parameters adopted in this work. The simulations were carried out with $n_{ch} = 30$ due to computational processing time constraints. This parameter has a direct influence on the efficiency of GNILC. With more frequency channels, there is more freedom for the method to fit for the independent components of emission (the foregrounds) without compromising the reconstruction of the wanted signal. The telescope is expected to work with more channels during the data collection, and this will improve the capability of the foreground cleaning method.

In line with the results of this work, we can say that GNILC can reconstruct the HI plus noise signal, for the IM BINGO experiment, with an (absolute) accuracy of ≈12% after five years of observation. This result may be improved by adding more horns to the telescope. The reconstruction is good even in the presence of systematics, such as $1/f$ noise, which was not considered in previous works (Olivari et al. 2016). This has been an encouraging result since this systematic will be present, to a great extent, in the real data and is the most complex contaminant to remove. Map-making methods can help to reduce the contribution of $1/f$ noise but at present are not optimized for our HI IM simulations. This is an important point because it indicates that it is preferable, where possible, to try to suppress $1/f$ noise in hardware, such as with the BINGO correlated channels, than to rely entirely on post-processing in software.

We note that the current implementation of GNILC in our analysis relies on a simple choice of the needlet bands, without any attempt at optimizing localization inside the small sky area observed by BINGO. The set was determined with equal intervals between peaks, with prioritization for high multipoles ($\ell > 100$), and is not definitive. In a future paper, for a more accurate cosmological signal recovery, a study to optimize their quantity and their distribution will be required. We intend to optimize the needlet localization inside the sky area observed by BINGO and anticipate some improvement of GNILC over a simple PCA since such localization will allow the number of principal components estimated by GNILC to vary inside the BINGO area. This is expected because GNILC estimates the number of principal components locally across the sky and, thus, allows the effective number of principal components to vary across the sky, while a PCA assumes a fixed number of principal components (e.g., three), all over the sky, which is a rough approximation given the expected variation in non-Gaussian foregrounds and signal-to-noise across the sky area observed by BINGO.

We can summarized the work presented in this paper as follows:

- Simulated cosmological signal with FLASK;
- Foreground modeling with galactic synchrotron, free-free, and AME;
- Simulated instrumental noise (thermal noise plus $1/f$ noise);
- Sky masking for different observational strategies;
- Cosmological HI signal recovery with GNILC;
- Comparison of simulated and recovered angular power spectra.

As the telescope construction proceeds, we will also work on the improvement of this pipeline to include other component separation methods and intend to address the following items in the near future:

- A more careful estimation of the errors in the recovered maps. One way to accomplish this is through Monte Carlo runs of different realizations of the observed sky. The main problem here is that it will require the simulation of a large number of different foreground skies, much larger than the number of available models that exist in the literature. A solution to this problem could be the use of some toy models for the spatial and frequency distribution of the different types of foreground emissions.
- Testing of different sets of needlets;
- Refining the $1/f$ noise model;
- Including more realistic terrestrial RFI measurements in the simulations;
- Including extragalactic point radio sources maps in the simulations.

The accomplishment of these points will allow us to produce more realistic simulations, which are a valuable tool for testing and verification of the quality of the component separation steps during the BINGO data analysis.

Acknowledgements

The BINGO project is supported by FAPESP grant 2014/07885-0. V. L. acknowledges the postdoctoral FAPESP grant 2018/02026-0. C.A.W. acknowledges CNPq through grant 313597/2014-6. T.V. acknowledges CNPq grant 308876/2014-8. F.B.A. acknowledges the UKRI-FAPESP grant 2019/05687-0, and FAPESP and USP for Visiting Professor Fellowships where this work has been developed. E. M. acknowledges a Ph.D. CAPES fellowship. F. V. acknowledges a CAPES

M.Sc. fellowship. C.P.N. thanks São Paulo Research Foundation (FAPESP) for financial support through grant 2019/06040-0, K.S.F.F. thanks São Paulo Research Foundation (FAPESP) for financial support through grant 2017/21570-0. Support from CNPq is gratefully acknowledged (E.A.). R.G.L. thanks CAPES (process 88881.162206/2017-01) and the Alexander von Humboldt Foundation for the financial support. A.R.Q., F.A.B., L.B., and M.V.S. acknowledge PRONEX/CNPq/FAPESQ-PB (Grant no. 165/2018). M.P. acknowledges funding from a FAPESP Young Investigator fellowship, grant 2015/19936-1. J.Z was supported by IBS under the project code, IBS-R018-D1. L.S. is supported by the National Key R&D Program of China (2020YFC2201600). M.R. acknowledges funding from the European Research Council Grant CMBSPEC (No. 725456). A.A.C. acknowledges financial support from the China Postdoctoral Science Foundation, grant number 2020M671611. B. W. and A.A.C. were also supported by the key project of NNSFC under grant 11835009. Some of the results in this paper have been derived using the HEALPix package (http://healpix.sourceforge.net) (Górski et al. 2005). This research made use of Astropy,[1] a community-developed core Python package for Astronomy (Astropy Collaboration et al. 2018), NumPy (Harris et al. 2020) and Healpy (Zonca et al. 2019).

References

Abdalla, E. et al. 2021a [arXiv:2107.01633]
Abdalla, F. B. et al. 2021b [arXiv:2107.01635]
Adam, R., Ade, P. A. R., Aghanim, N., et al. 2016, A&A, 594, A10
Albrecht, A., Bernstein, G., Cahn, R., et al. 2006, arXiv e-prints [astro-ph/0609591]
Alonso, D., Bull, P., Ferreira, P. G., & Santos, M. G. 2014, Monthly Notices of the Royal Astronomical Society, 447, 400
Ansari, R., Campagne, J. E., Colom, P., et al. 2012, Astron. Astrophys., 540, A129
Astropy Collaboration, Price-Whelan, A. M., Sipőcz, B. M., et al. 2018, AJ, 156, 123
Battye, R. A., Browne, I. W. A., Dickinson, C., et al. 2013, Mon. Not. R. Astron. Soc., 434, 1239
Bigot-Sazy, M. A., Dickinson, C., Battye, R. A., et al. 2015, Mon. Not. R. Astron. Soc., 454, 3240
Blake, C. & Glazebrook, K. 2003, The Astrophysical Journal, 594, 665
Chang, T.-C., Pen, U.-L., Bandura, K., & Peterson, J. B. 2010, Nature, 466, 463
Costa, A. A. et al. 2021 [arXiv:2107.01639]
de Gasperis, G., Buzzelli, A., Cabella, P., de Bernardis, P., & Vittorio, N. 2016, A&A, 593, A15
De Oliveira-Costa, A., Tegmark, M., Gaensler, B. M., et al. 2008, Mon. Not. R. Astron. Soc., 388, 247
Delabrouille, J., Betoule, M., Melin, J. B., et al. 2013, Astron. Astrophys., 553, A96
Dickinson, C., Ali-Haïmoud, Y., Barr, A., et al. 2018, New Astron. Rev., 80, 1
Dickinson, C., Davies, R. D., & Davis, R. J. 2003, Mon. Not. R. Astron. Soc., 341, 369
Eisenstein, D. J., Zehavi, I., Hogg, D. W., et al. 2005, ApJ, 633, 560
Evans, I. D. 2017, Master's thesis, The University of Manchester (United Kingdom)
Flaugher, B. 2005, Int. J. Mod. Phys. A, 20, 3121
Fornazier, K. S. F. et al. 2021 [arXiv:2107.01637]
Furlanetto, S. R., Oh, S. P., & Briggs, F. H. 2006, Phys. Rep., 433, 181
Giardino, G., Banday, A. J., Górski, K. M., et al. 2002, A&A, 387, 82
Górski, K. M., Hivon, E., Banday, A. J., et al. 2005, Astrophys. J., 622, 759
Hall, A., Bonvin, C., & Challinor, A. 2013, Phys. Rev. D, 87, 064026
Harper, S. E., Dickinson, C., Battye, R. A., et al. 2018, Mon. Not. R. Astron. Soc., 478, 2416
Harris, C. R., Millman, K. J., van der Walt, S. J., et al. 2020, Nature, 585, 357
Haslam, C. G. T., Salter, C. J., Stoffel, H., & Wilson, W. E. 1982, Astron. Astrophys. Suppl., 47, 1
Janssen, M. A., Scott, D., White, M., et al. 1996, arXiv e-prints [arXiv:astro-ph/9602009]
Jonas, J. L., Baart, E. E., & Nicolson, G. D. 1998, MNRAS, 297, 977
Lah, P., Pracy, M. B., Chengalur, J. N., et al. 2009, Mon. Not. R. Astron. Soc., 399, 1447
Loureiro, A. et al. 2019, Mon. Not. Roy. Astron. Soc., 485, 326
Maino, D., Burigana, C., Górski, K. M., Mand olesi, N., & Bersanelli, M. 2002, Astron. Astrophys., 387, 356
Masui, K. W., Switzer, E. R., Banavar, N., et al. 2013, Astrophys. J. Lett., 763, L20
McLeod, M., Balan, S. T., & Abdalla, F. B. 2017, Monthly Notices of the Royal Astronomical Society, 466, 3558
Miville-Deschênes, M. A., Ysard, N., Lavabre, A., et al. 2008, Astron. Astrophys., 490, 1093
Natoli, P., de Gasperis, G., Gheller, C., & Vittorio, N. 2001, A&A, 372, 346
Olivari, L. C., Remazeilles, M., & Dickinson, C. 2016, Mon. Not. R. Astron. Soc., 456, 2749
Paine, S. 2019, The am atmospheric model
Paradis, D., Dobashi, K., Shimoikura, T., et al. 2012, A&A, 543, A103
Peterson, J. B., Bandura, K., & Pen, U. L. 2006, ArXiv Astrophysics e-prints [astro-ph/0606104]
Planck Collaboration, Ade, P. A. R., Aghanim, N., et al. 2016a, Astron. Astrophys., 594, A25
Planck Collaboration, Aghanim, N., Akrami, Y., et al. 2020, Astron. Astrophys., 641, A6
Planck Collaboration, Aghanim, N., Ashdown, M., et al. 2016b, A&A, 596, A109
Pritchard, J. R. & Loeb, A. 2012, Rep. Prog. Phys., 75, 086901
Reich, P. & Reich, W. 1986, Astron. Astrophys. Suppl., 63, 205
Remazeilles, M., Delabrouille, J., & Cardoso, J.-F. 2011, Monthly Notices of the Royal Astronomical Society, 418, 467
Remazeilles, M., Dickinson, C., Banday, A. J., Bigot-Sazy, M.-A., & Ghosh, T. 2015, Mon. Not. R. Astron. Soc., 451, 4311
Sánchez, C., Carrasco Kind, M., Lin, H., et al. 2014, Mon. Not. R. Astron. Soc., 445, 1482
Seo, H.-J., Dodelson, S., Marriner, J., et al. 2010, ApJ, 721, 164
Silsbee, K., Ali-Haïmoud, Y., & Hirata, C. M. 2011, Monthly Notices of the Royal Astronomical Society, 411, 2750
Switzer, E. R., Chang, T. C., Masui, K. W., Pen, U. L., & Voytek, T. C. 2015, ApJ, 815, 51
Switzer, E. R., Masui, K. W., Bandura, K., et al. 2013, Mon. Not. R. Astron. Soc., 434, L46
Weinberg, D. H., Mortonson, M. J., Eisenstein, D. J., et al. 2013, Phys. Rep., 530, 87
Wilson, T. L., Rohlfs, K., & Hüttemeister, S. 2013, Tools of Radio Astronomy (Springer-Verlag)
Wolleben, M., Landecker, T. L., Reich, W., & Wielebinski, R. 2006, A&A, 448, 411
Wuensche, C. A. & BINGO Collaboration. 2019, in Journal of Physics Conference Series, Vol. 1269, Journal of Physics Conference Series, 012002
Wuensche, C. A. et al. 2021 [arXiv:2107.01634]
Xavier, H. S., Abdalla, F. B., & Joachimi, B. 2016, Mon. Not. R. Astron. Soc., 459, 3693
Zhang, J. et al. 2021 [arXiv:2107.01638]
Zonca, A., Singer, L., Lenz, D., et al. 2019, Journal of Open Source Software, 4, 1298

[1] http://www.astropy.org